Uncertainty Analysis and Robust Design of Low-Boom Concepts using Atmospheric Adjoints

Sriram K. Rallabhandi [*]

National Institute of Aerospace, Hampton, VA, 23666

Thomas K. West[†] and Eric J. Nielsen[‡]

NASA Langley Research Center, Hampton, VA, 23681

This paper seeks to quantify the uncertainty associated with atmospheric conditions when propagating shaped pressure disturbances due to a low-boom supersonic aircraft. A discrete adjoint formulation is used to obtain sensitivities of the boom metrics to atmospheric inputs such as temperature, wind, and relative humidity distributions in addition to deterministic inputs such as the near-field pressure distribution. This study uses a polynomial chaos theory approach to couple these adjoint-derived gradients with uncertainty quantification to enable robust design by using gradient-based optimization techniques. The effectiveness of this approach is demonstrated over an axisymmetric body of revolution. Results show that the mean and standard deviation of sonic boom loudness are simultaneously reduced using robust optimization. Unlike the conventional optimization approaches, the robust optimization approach has the added benefit of generating probability distributions of the sonic boom metrics.

Nomenclature

α	Deterministic coefficient in the polynomial chaos expansion
β	$1 + \frac{\gamma-1}{2}$
β_n	Lagrange multiplier for absorption
χ	Non-dimensional distance
δ	Truncation error
ϵ	Wind effect on ray acoustics
η	Non-dimensional longitudinal location
Γ	Non-dimensional thermo-viscous parameter
γ	Ratio of specific heats, 1.4
$\gamma_{0,n}$	Lagrange multiplier for nitrogen relaxation
$\gamma_{1,n}$	Lagrange multiplier for oxygen relaxation
λ_n	Lagrange multiplier for nonlinearity
μ	Mean
ϕ	Azimuthal angle for propagation
Ψ	Random basis function
ρ	Atmospheric density
ρ_h	Density at an arbitrary location along the ray
σ	Standard deviation
$\theta_{\nu,1-2}$	Non-dimensional relaxation time parameters
ξ	Standard input random variable

[*]Associate Research Fellow, National Institute of Aerospace, Associate Fellow AIAA
[†]Aerospace Engineer, Vehicle Analysis Branch, Systems Analysis and Concepts Directorate, Member AIAA
[‡]Research Scientist, Computational Aerosciences Branch, Research Directorate, Associate Fellow AIAA

American Institute of Aeronautics and Astronautics

c	Speed of sound
$C_{\nu,1-2}$	Non-dimensional dispersion
c_h	Speed of sound at an arbitrary location along the ray
D	Vector of design variables
G	Ray tube area
h	Altitude at an arbitrary location along the ray
H_i	Input altitudes of atmospheric temperature profile
J	Objective function
J_N	Non-deterministic objective function
k_n	Scaling factor due to ray-tube spreading and stratification
L	Lagrangian
M	Cruise Mach number
m	percent mole fraction of water vapor in air
n	Number of random dimensions
N_{TP}	Number of test points
N_s	Number of samples
N_t	Number of terms in a total-order polynomial chaos expansion
nh	Number of atmospheric profile altitude, relative humidity pairs
nt	Number of atmospheric profile altitude, temperature pairs
nwx	Number of atmospheric profile altitude, X-wind pairs
nwy	Number of atmospheric profile altitude, Y-wind pairs
p	Pressure waveform during propagation
P	Number of output modes
P_h	Pressure at an arbitrary location along the ray
P_{sat}	Saturation vapor pressure
q, r, t	Intermediate pressure waveforms
R	Gas constant, 287.26 J/KgK
RH_i	Input relative humidities of atmospheric humidity profile
s	Order of polynomial expansion
T_h	Temperature at an arbitrary location along the ray
T_i	Input temperatures of atmospheric temperature profile
U	Atmospheric variables T_i, RH_i, WX_i, WY_i
u_n	X-wind velocity along the wave normal direction
V	Atmospheric variables H_i, ZH_i, WXH_i, WYH_i
v_n	Y-wind velocity along the wave normal direction
W	Wind at an arbitrary location along the ray
WX_i	Input winds of atmospheric wind X-profile
WXH_i	Input altitudes of atmospheric wind X-profile
WY_i	Input winds of atmospheric wind Y-profile
WYH_i	Input altitudes of atmospheric wind Y-profile
x	Independent input random variable
x_i	Longitudinal ranges along each ray $\forall i \in [1,4]$ of the ray tube
Y	Response value
y_i	Lateral ranges along each ray $\forall i \in [1,4]$ of the ray tube
z_i	Vertical distances along each ray $\forall i \in [1,4]$ of the ray tube
ZH_i	Input altitudes of atmospheric humidity profile

Subscripts

0	Starting conditions
i	running iteration counter
l	Sensitivity index w.r.t. temperature profile
n	Propagation iteration counter
r	Sensitivity index w.r.t. relative humidity profile
x	Longitudinal component
y	Lateral component

American Institute of Aeronautics and Astronautics

I.   Introduction and Motivation

Sonic boom remains a critical concern for commercial supersonic overland flight. Since the successful demonstration of the DARPA Shaped Sonic Boom Demonstrator (SSBD),[1] the past decade has seen multiple research efforts[2,3,4,5,6,7,8,9] toward mitigating the adverse impact of sonic boom. Numerical tools and methods employed for boom mitigation have seen tremendous improvements not only due to ever increasing computational power, but also through the use of advanced techniques such as adjoint-based methods. Multiple studies have demonstrated the capability of adjoint-based methods to optimize near-field pressure waveforms,[2,10,11] ground-based boom metrics,[8] as well as equivalent area metrics.[5,9] A fundamental assumption in these studies has been that the atmospheric temperature, humidity and wind distributions are fixed to standard atmospheric[12] profiles that do not vary with time. In reality, boom metrics on the ground are based on the prevalent atmospheric conditions and there is a need to quantify this uncertainty under varying atmospheric conditions so it may be considered during the design process.

The primary objective of this paper is to develop a discrete adjoint methodology to obtain sensitivities of boom metrics with respect to atmospheric temperature, relative humidity and wind profiles, and use them for robust design of an underlying concept under varying atmospheric conditions. The propagation algorithm used in this study is sBOOM.[13] The ultimate goal is to design aircraft concepts while accounting for the aleatory uncertainty inherent in atmospheric propagation.

In robust design, probability distributions are placed on uncertain parameters and appropriate techniques are used to obtain distributions of the output quantities of interest. While stochastic techniques such as Monte Carlo methods may be used without the need for sensitivities, such approaches can become prohibitively expensive due to the numerous function evaluations needed to generate usable probability distributions. Despite this computational expense, the sensitivities of moments (mean and standard deviation) from probability distributions is not known. In the interest of minimizing computational expense, a non-intrusive polynomial chaos surrogate modeling approach[14] is used to perform uncertainty quantification. This has the additional advantage of providing analytical mean and standard deviation sensitivities. The optimization problem is recast to a robust design objective as given in Eq. 1, where J_N is a non-deterministic function of the objective chosen for optimization.

$$J_N = \mu(J) + \sigma(J) \tag{1}$$

The paper is organized as follows: Section II provides a brief derivation of changes needed in the boom adjoint formulation to account for atmospheric sensitivities. Section III provides verification of adjoint sensitivities by using complex variables. Section IV discusses polynomial chaos formulation; and sections V, VI and VII detail the CFD integration, optimization setup, and results, respectively. Finally, conclusions and future work will be discussed.

II.   Extension to Existing Theory

The discrete adjoint formulation derived in this section is based on a similar implementation developed in Refs. 8 and 9. In this paper, specific details that pertain to computation of sensitivities with respect to atmospheric parameters are provided. The primary difference occurs in the independent variable vector D, which represented the near-field pressure or equivalent area distribution in the old formulation, now represents the atmospheric temperature pairs $(H_i, T_i) \forall i \in [1, nt]$, relative humidity pairs $(ZH_i, RH_i) \forall i \in [1, nh]$, as well as X and Y wind pairs, $(WXH_i, WX_i) \forall i \in [1, nwx]$, and $(WYH_i, WY_i) \forall i \in [1, nwy]$. This makes the length of the independent design variable vector to be $2(nt + nh + nwx + nwy)$.

Following the formulation of previous papers, the Lagrangian corresponding to a chosen objective, J, is written in Eq. 2, where k_n is the Blokhintzev invariant[15] scaling factor given by $\sqrt{\frac{\rho_0 c_0 G}{\rho c G_0} \frac{\epsilon}{\epsilon_0}}$. The details of the matrix terms are provided in the Appendix. Taking the derivative of the Lagrangian with respect to D results in Eq. 3. Contrary to the previous boom-adjoint formulations, the relevant matrices during

American Institute of Aeronautics and Astronautics

propagation now depend on the design variable vector D, and hence matrix derivative terms now appear in the derivative of the Lagrangian.

$$L(p,q,r,t,D) = J(p_N, D) + \sum_{n=2}^{N} \gamma_{0,n}^T \left[A_n q_n - k_n B_n p_{n-1} \right] + \sum_{n=1}^{N} \gamma_{1,n}^T \left[A_{n,2} r_n - B_{n,2} q_n \right]$$
$$+ \sum_{n=1}^{N} \beta_n^T \left[A_{n,3} t_n - B_{n,3} r_n \right] + \sum_{n=1}^{N} \lambda_n^T \left[p_n - f_n(t_n, D) \right] + \gamma_{0,1}^T \left[A_1 q_1 - k_1 B_1 p_0(D) \right] \tag{2}$$

$$\frac{dL}{dD} = \left[\frac{\partial J_N}{\partial D} + \frac{\partial J_N}{\partial p_N} \frac{\partial p_N}{\partial D} \right] + \sum_{n=1}^{N} \gamma_{1,n}^T \left[A_{n,2} \frac{\partial r_n}{\partial D} + \frac{\partial A_{n,2}}{\partial D} r_n - B_{n,2} \frac{\partial q_n}{\partial D} - \frac{\partial B_{n,2}}{\partial D} q_n \right]$$
$$+ \sum_{n=2}^{N} \gamma_{0,n}^T \left[A_n \frac{\partial q_n}{\partial D} + \frac{\partial A_n}{\partial D} q_n - k_n B_n \frac{\partial p_{n-1}}{\partial D} - \frac{\partial k_n}{\partial D} B_n p_{n-1} - k_n \frac{\partial B_n}{\partial D} p_{n-1} \right]$$
$$+ \sum_{n=1}^{N} \beta_n^T \left[A_{n,3} \frac{\partial t_n}{\partial D} + \frac{\partial A_{n,3}}{\partial D} t_n - B_{n,3} \frac{\partial r_n}{\partial D} - \frac{\partial B_{n,3}}{\partial D} r_n \right] + \sum_{n=1}^{N} \lambda_n^T \left[\frac{\partial p_n}{\partial D} - \frac{\partial f_n}{\partial D} - \frac{\partial f_n}{\partial t_n} \frac{\partial t_n}{\partial D} \right] \tag{3}$$
$$+ \gamma_{0,1}^T \left[A_1 \frac{\partial q_1}{\partial D} + \frac{\partial A_1}{\partial D} q_1 - k_1 B_1 \frac{\partial p_0}{\partial D} - \frac{\partial k_1}{\partial D} B_1 p_0 - k_1 \frac{\partial B_1}{\partial D} p_0 \right]$$

Adjoint equations are extracted as in previous formulations[8,9] and the resulting terms, given in Eq. 4, allow computation of the relevant uncertainty sensitivities. Note that this expression is quite involved compared to the gradient expression for computing the deterministic sensitivities (See Eq. 19 from Ref 8).

$$\frac{dL}{dD} = \sum_{n=2}^{N} \gamma_{0,n}^T \left[\frac{\partial A_n}{\partial D} q_n - \frac{\partial k_n}{\partial D} B_n p_{n-1} - k_n \frac{\partial B_n}{\partial D} p_{n-1} \right]$$
$$+ \sum_{n=1}^{N} \gamma_{1,n}^T \left[\frac{\partial A_{n,2}}{\partial D} r_n - \frac{\partial B_{n,2}}{\partial D} q_n \right] + \sum_{n=1}^{N} \beta_n^T \left[\frac{\partial A_{n,3}}{\partial D} t_n - \frac{\partial B_{n,3}}{\partial D} r_n \right] \tag{4}$$
$$- \sum_{n=1}^{N} \lambda_n^T \left[\frac{\partial f_n}{\partial D} \right] + \gamma_{0,1}^T \left[\frac{\partial A_1}{\partial D} q_1 - \frac{\partial k_1}{\partial D} B_1 p_0 - k_1 \frac{\partial B_1}{\partial D} p_0 - k_1 B_1 \frac{\partial p_0}{\partial D} \right]$$

In order to get the matrix derivative terms, ray acoustics are differentiated to obtain sensitivities of several quantities, notably:

1. Atmospheric properties

2. Atmospheric absorption and relaxation effects

3. Longitudinal and lateral ranges

4. Ray tube areas, wind effects

Sensitivities at each succeeding level require preceding level sensitivities as a prerequisite.

II.A. Differentiating Atmospheric Properties

A schematic of the ray as it travels from aircraft to ground through the atmosphere is depicted in Fig. 1. The path taken by the ray is determined by geometric ray acoustic equations.[16] Given the atmospheric temperature profile as altitude and temperature pairs $(H_i, T_i) \forall i \in [1, nt]$, the atmospheric temperature (T_h) at any intermediate point on the ray is a linear interpolation between the temperatures at the enclosing
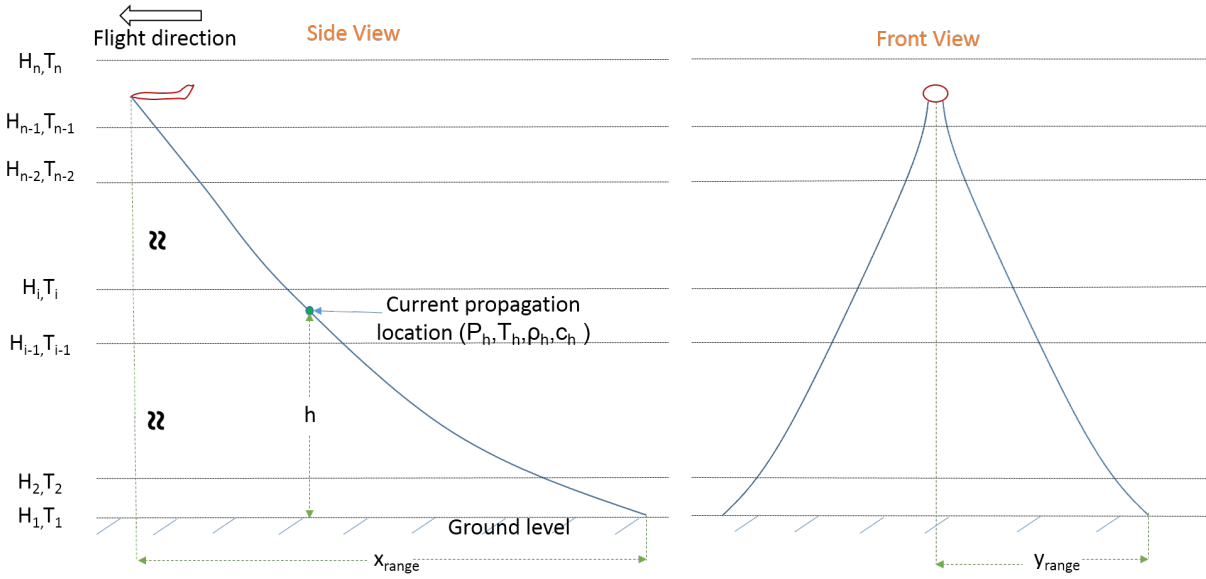
Figure 1. Side view of ray propagation through the atmosphere.

altitudes $[H_{i-1}, H_i]$. Sensitivities of T_h with respect to atmospheric temperature profile inputs are calculated analytically by differentiating the underlying linear interpolation. Because speed of sound is dependent solely on the temperature via $c_h = \sqrt{\gamma R T_h}$, its sensitivity can also be obtained.

The pressures at the input altitudes $H_i \forall i \in [1, nt]$ need to be determined before atmospheric pressures at intermediate locations are obtained. These pressures are calculated based on the hydrostatic equation, which may be differentiated to obtain pressure sensitivities at the input altitudes, H_i. The pressures and their sensitivities at the intermediate ray locations can then be computed. Temperature sensitivities have strong local support depending on immediately preceding and succeeding altitude and temperature values enclosing the current location on the ray. In contrast, pressure (and consequently density) sensitivities have non-zero values from the ground level and up to the position immediately above the current intermediate location of the ray. After this step, we would have $[\frac{dT_h}{dl}, \frac{dP_h}{dl}, \frac{d\rho_h}{dl}, \frac{dc_h}{dl}]$ where $l \in [H_i, T_i] \forall i \in [1, nt]$. Atmospheric properties do not depend on relative humidity or winds, therefore their corresponding sensitivities are zero.

II.B. Differentiating Atmospheric Absorption and Relaxation Effects

During propagation, atmospheric absorption formulae[17] are used to account for the thermo-viscous attenuation and vibrational relaxation losses due to nitrogen and oxygen, which are functions of temperature, pressure, and relative humidity. These quantities are numerically differentiated to obtain sensitivities of these quantities with respect to atmospheric temperature, wind and relative humidity profiles. Due to their dependence on atmospheric pressures, these sensitivities do not exhibit local support and are non-zero with respect to all the altitudes from the ground level to the location in the atmospheric profile immediately above the current ray point. The absorption coefficient is given by Eq. 5, where $P_r = 101.325$ kPa is the reference pressure, and $T_r = 293.15K$ is the reference temperature. Its sensitivity is numerically computed by using Eq. 6, where $l \in [H_i, T_i] \forall i \in [1, nt]$.

$$A_{cr} = 1.84 \times 10^{-11.0} \frac{P_r}{P_h} \sqrt{\frac{T_h}{T_r}} \tag{5}$$

$$\frac{dA_{cr}}{dl} = 1.84 \times 10^{-11.0} \frac{P_r}{\sqrt{T_r}} \frac{0.5 P_h \frac{dT_h}{dl} - T_h \frac{dP_h}{dl}}{P_h^2 \sqrt{T_h}} \tag{6}$$

The vibrational relaxation has two terms. The first term depends solely on the temperature profile, and its sensitivity is calculated as for the above term. The second term is given by Eq. 7 for nitrogen,

American Institute of Aeronautics and Astronautics

where the percent mole fraction of water vapor in air (m) depends on relative humidity via $m = \frac{(RH)P_{sat}}{P_h}$. The derivative terms with respect to temperature and relative humidity profiles are given by Eqs. 8 and 9, respectively. Other relevant terms are similarly computed.

$$f_{v,N} = \frac{P_h}{P_r}(24 + 4.04 \times 10^{4.0} m \frac{0.02 + m}{0.391 + m}) \tag{7}$$

$$\frac{df_{v,N}}{dl} = \frac{24}{P_r}\frac{dP_h}{dl} + \frac{4.04 \times 10^{4.0}}{P_r}\frac{(0.391 + m)\frac{dP_h}{dl}m(0.02 + m) + P_h(0.02 + 2m)\frac{dm}{dl} - P_h m(0.02 + hm)\frac{dm}{dl}}{(0.391 + m)^2} \tag{8}$$

$$\frac{df_{v,N}}{dr} = 4.04 \times 10^{4.0}\frac{P_h}{P_r}\frac{(0.391 + m)(0.02 + m)\frac{dm}{dr} - (0.02m + m^2)\frac{dm}{dr}}{(0.391 + m)^2} \tag{9}$$

II.C. Differentiating Longitudinal and Lateral Ranges

Obtaining the lateral range sensitivities involves differentiating multiple quantities such as propagation angles, ray vectors, Snell's constant, wind velocities, along with the above mentioned quantities with respect to all atmospheric profile inputs. Once these are obtained, the incremental longitudinal and lateral ranges, for each of the four rays comprising the ray tube may be differentiated to obtain their sensitivity with respect to atmospheric parameters. These incremental quantities are summed during propagation of aircraft disturbances along ray tubes from cruise altitude to ground. This results in sensitivities of the longitudinal and lateral ranges with respect to atmospheric temperature and wind profiles.

II.D. Differentiating Ray Tube Areas

Once sensitivities of longitudinal/lateral ranges, ray vectors, and angles with respect to all relevant atmospheric profiles are obtained, the ray tube area calculation is differentiated to obtain the sensitivities with respect to the relevant atmospheric quantities. This includes calculation of the sensitivity of the unit vector along the wave normal direction $\hat{n}$. These values are then used in a discrete-adjoint gradient formulation (see Eq. 4) to extrapolate these sensitivities to the ground.

II.E. Demonstration Example

In order to demonstrate the use of these atmospheric sensitivities in robust design optimization, sample atmospheric temperature, and wind distributions are given in tables 1, 2, and 3, respectively. The temperature profile follows the ISO standard atmosphere model with arbitrarily chosen wind distributions. The relative humidity profile follows ANSI S1.26-1995, Appendix C.[17] The relative humidity profile is truncated at 45000 ft amounting to 46 altitude, relative humidity pairs. With this choice of atmospheric profiles, the number of variables for atmospheric sensitivity calculation is $2 \times (3 + 3 + 11 + 46) = 126$. The formulation is not limited to these distributions; the user has the freedom to pick any arbitrary atmospheric profile with the only caveat being that the computational time will increase as the size of the uncertain variable vector increases.

Table 1. Atmospheric temperature table.

i	Altitude (m)	Temperature (^oF)
1	0.0	59.0
2	11000.0	-69.7
3	20000.0	-69.7

Table 2. Atmospheric x-wind table.

i	Altitude (m)	X-Wind (m/s)
1	0.0	0.0
2	5000.0	20.0
3	20000.0	30.0

With the above atmospheric profile inputs, an arbitrary near-field is propagated from 45000.0 ft to the ground (MSL) and the sensitivity of ray tube areas with respect to T_i and $H_i \forall i \in [1, nt]$ are plotted in Figs.

American Institute of Aeronautics and Astronautics

Table 3. Atmospheric y-wind table.

i	Altitude (m)	Y-Wind (m/s)	i	Altitude (m)	Y-Wind (m/s)
1	0.0	0.0	7	13950.0	16.0
2	2000.0	10.0	8	14000.0	14.0
3	4000.0	12.0	9	16000.0	16.0
4	6000.0	14.0	10	18000.0	18.0
5	8000.0	16.0	11	20000.0	20.0
6	13700.0	18.0			

2 and 3, respectively. As the distance along the ray tube increases, the disturbance propagates towards the ground from the source (aircraft location) and the ray tube area (G) increases as shown by the solid line. Because the starting location of propagation is between atmospheric temperature layers 2 and 3, the sensitivity with respect to T_1 starts off at zero and becomes non-zero when the ray tube crosses into the first atmospheric temperature layer. As the ray moves downwards, the sensitivity with respect to T_3 gradually drops, as expected. The sensitivity with respect to T_1 initially drops owing to the effect of Snell's constant, but then gradually increases as the ray approaches the ground.

Because the propagation starts in a constant temperature layer, all sensitivities with respect to H_i are zero to begin with. As soon as the ray moves into the subsequent layer, the sensitivities with respect to H_1 and H_2 become non-zero and stay that way through the end of propagation. Sensitivity with respect to H_3 remains zero through out.
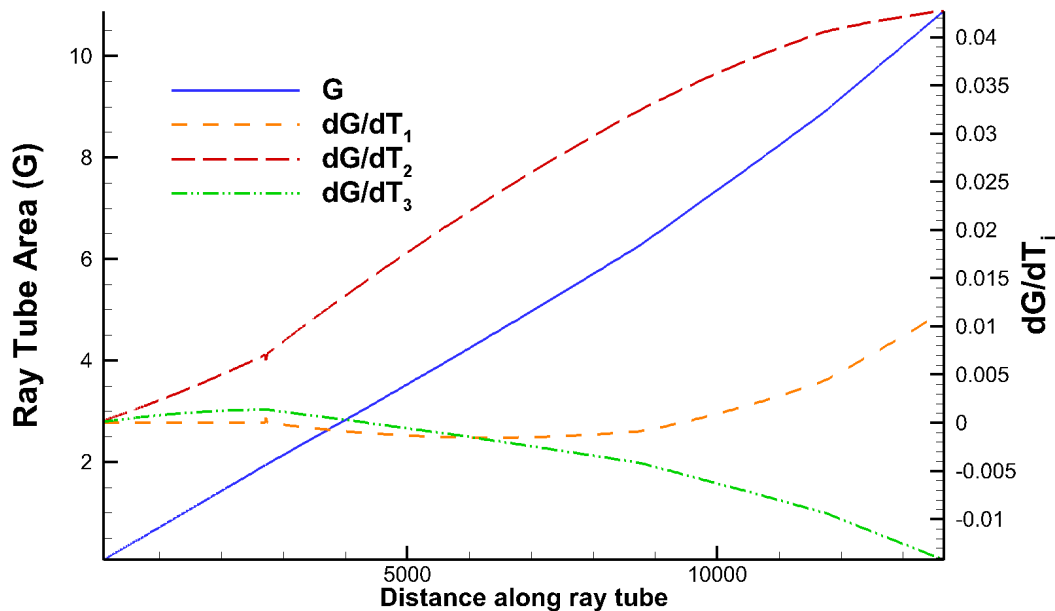
Figure 2. Sensitivities of ray tube areas wrt T_i along the ray.

Finally, all relevant derivative terms are used to compute the sensitivities of the ground A-weighted loudness levels with respect to the atmospheric parameters. This information is plotted in Fig. 4. A few observations can be made: the sensitivities with respect to altitude variables are almost two orders of magnitude smaller than those with respect to profile variables. The relative humidity sensitivities seem smaller compared to temperature and wind sensitivities; however the relative humidity profile has much finer resolution than the other profiles and therefore the effect of the sensitivities is dispersed across multiple values. The relative humidity between 4 and 10 km seem to have appreciably large sensitivities compared to altitudes out of this range.

American Institute of Aeronautics and Astronautics
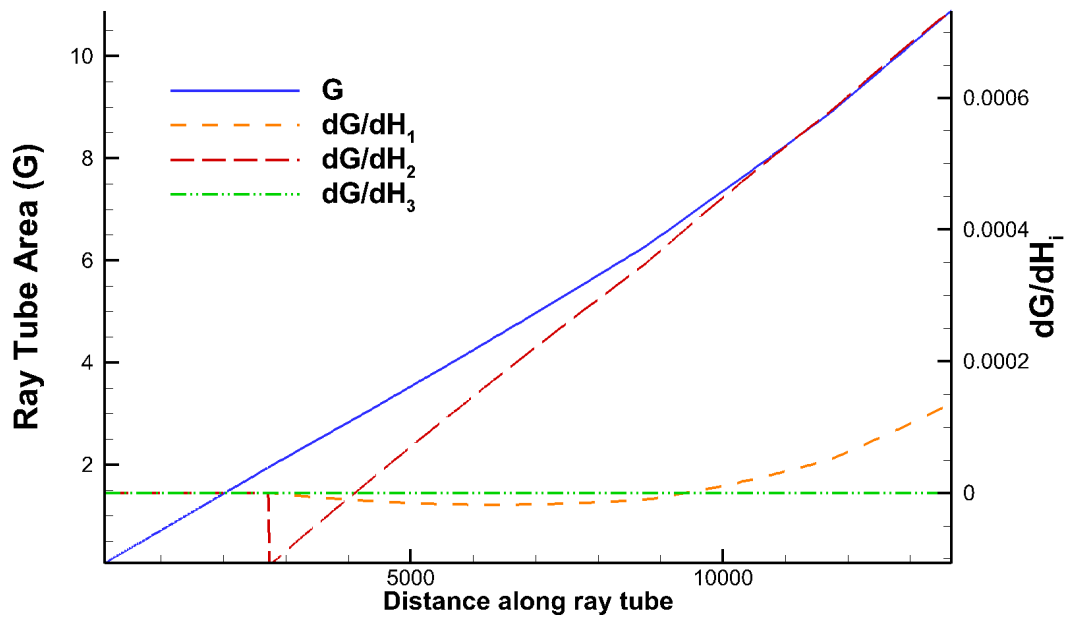
Figure 3. Sensitivities of ray tube areas wrt H_i along the ray.

III.   Verification of Adjoint Sensitivities

To verify that the sensitivity values obtained from adjoint calculations are correct, a complex variable version of the propagation algorithm[8] has been extended to include atmospheric profile parameters. The use of complex step approach[18,19] is common practice for discrete-adjoint gradient verification. The derivatives of appropriate cost functional with respect to the chosen design variables are calculated with an imaginary step size of 10^{-50}. As an example case, an arbitrary off-body pressure waveform is propagated to the ground from an altitude of 45000.0 ft by using the atmospheric profiles from the previous section.

Figure 4. Sensitivities of ground loudness to uncertain atmospheric parameters.

American Institute of Aeronautics and Astronautics

III.A.   Sensitivity of Ranges to Temperature Profile

Table 4 compares the adjoint and complex variable gradients of the longitudinal range (X) with respect to the atmospheric temperature profile propagated at $\phi = 0$ deg. The results obtained by using the discrete-adjoint implementation exhibit excellent agreement with the complex-variable sensitivities. The lateral range sensitivities, not shown here, exhibit similar agreement.
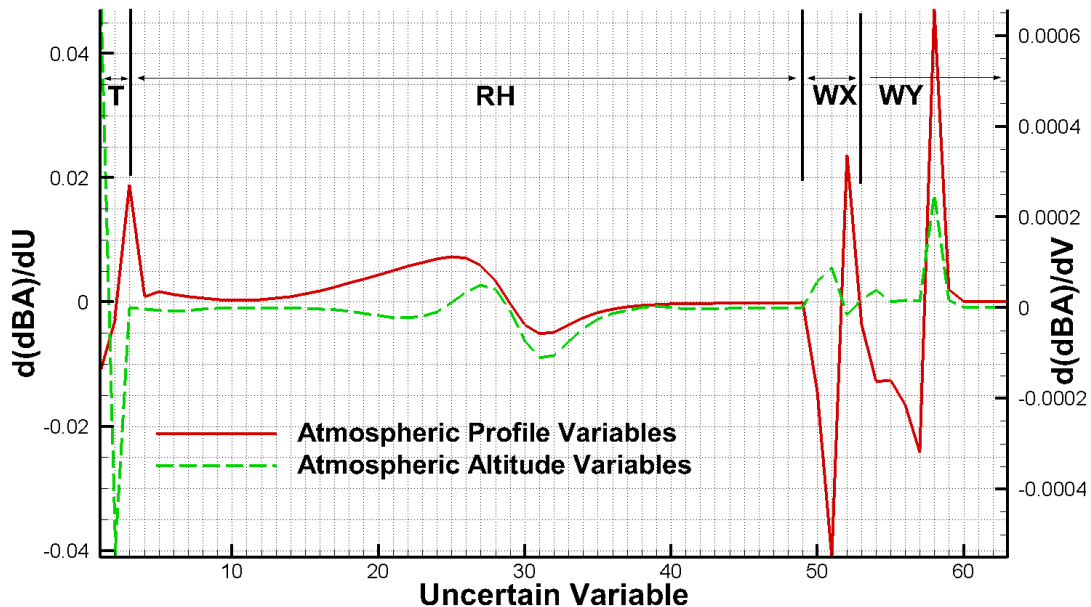
Table 4. Comparison of the adjoint and complex variable gradients of longitudinal range with respect to atmospheric temperature profile.

i	Adjoint $\frac{dX}{dH_i}$	Complex $\frac{dX}{dH_i}$	Adjoint $\frac{dX}{dT_i}$	Complex $\frac{dX}{dT_i}$
1	3.6411515035386e-01	3.6411515035386e-01	3.1120953021697e+01	3.1120953021697e+01
2	3.5756795853379e-01	3.5756795853379e-01	-1.9552471410692e+01	-1.9552471410692E+01
3	0.0	0.0	-2.4785035986202e+01	-2.4785035986202e+01

III.B.   Sensitivity of Ray Tube Area to Temperature Profile

Table 5 compares the sensitivities of the final ray tube areas with respect to the temperature profile and shows similarly good agreement with the values computed using the complex step.

Table 5.   Comparison of the adjoint and complex variable gradients of final ray tube area with respect to atmospheric temperature profile.

i	Adjoint $\frac{dG}{dH_i}$	Complex $\frac{dG}{dH_i}$	Adjoint $\frac{dG}{dT_i}$	Complex $\frac{dG}{dT_i}$
1	-1.321129416e-05	-1.321129367e-05	-1.12917044154e-03	-1.12917044122e-03
2	2.7231615202e-04	2.7231615202e-04	3.555981669993e-02	3.555981669740E-02
3	0.0	0.0	2.88949068962e-03	2.88949068922E-003

III.C.   Sensitivity of Boom Loudness on Ground to Atmospheric Profiles

Tables 6, 7, 8 and 9 compare the adjoint and complex sensitivities of the A-weighted sonic boom loudness on the ground with respect to temperature, relative humidity, longitudinal winds, and lateral winds, respectively. These show the adjoint sensitivities to be sufficiently accurate for robust shape optimization.

Table 6. Comparison of the adjoint and complex variable gradients of loudness with respect to atmospheric temperature profile.

i	Adjoint $\frac{d(dBA)}{dH_i}$	Complex $\frac{d(dBA)}{dH_i}$	Adjoint $\frac{d(dBA)}{dT_i}$	Complex $\frac{d(dBA)}{dT_i}$
1	-2.65520482293e-03	-2.655204826526e-03	-3.1715456323555e-01	-3.1715456305859e-01
2	-1.50109609843e-03	-1.50109609746e-03	-1.0220917238573e-01	-1.0220917227936e-01
3	0.0	0.0	8.31945048719e-03	8.31945047897e-03

IV.   Robust Design via Polynomial Chaos

This section details integration of the robust adjoint-based approach with stochastic expansions based on polynomial chaos theory for efficient design of low boom configurations under conditions of atmospheric uncertainty. The first section outlines the approach to adjoint-based design under aleatory uncertainty. The second section details the non-intrusive polynomial chaos formulation along with two alternative approaches for point-collocation. The third section describes the moments and sensitivities that can be obtained from the polynomial chaos expansion (PCE), which are required for adjoint-based robust design. The last section describes the design optimization approach used in this study.

American Institute of Aeronautics and Astronautics

Table 7. Comparison of the adjoint and complex variable gradients of loudness with respect to atmospheric relative humidity profile.

i	Adjoint $\frac{d(dBA)}{dZH_i}$	Complex $\frac{d(dBA)}{dZH_i}$	Adjoint $\frac{d(dBA)}{dRH_i}$	Complex $\frac{d(dBA)}{dRH_i}$
1	-3.31340788e-06	-3.31340850e-06	1.15583996055e-03	1.15584018002e-03
5	1.138961647e-05	1.138961270e-05	-2.19573375454e-03	-2.19573398795e-03
15	1.003778893e-05	1.003778657e-05	-3.89453657775e-03	-3.89453667621e-03
25	-4.08028872e-06	-4.08029035e-06	-3.1340648204e-04	-3.1340659837e-04
45	-5.573018e-08	-5.573029e-08	-1.443489020e-05	-1.4434919046e-05

Table 8. Comparison of the adjoint and complex variable gradients of loudness with respect to atmospheric X-wind profile.

i	Adjoint $\frac{d(dBA)}{dWXH_i}$	Complex $\frac{d(dBA)}{dWXH_i}$	Adjoint $\frac{d(dBA)}{dWX_i}$	Complex $\frac{d(dBA)}{dWX_i}$
1	1.6883853603e-04	1.6883854879e-04	-4.220963400862e-02	-4.220963718547e-02
2	1.1105345796e-04	1.1105433172e-04	-2.876100869696e-02	-2.876100356143e-02
3	-1.396746132e-05	-1.396746828e-05	2.095120198323e-02	2.095120211186e-02

Table 9. Comparison of the adjoint and complex variable gradients of loudness with respect to atmospheric Y-wind profile.

i	Adjoint $\frac{d(dBA)}{dWYH_i}$	Complex $\frac{d(dBA)}{dWYH_i}$	Adjoint $\frac{d(dBA)}{dWY_i}$	Complex $\frac{d(dBA)}{dWY_i}$
2	1.47401661e-06	1.47401704e-06	-5.3625057572e-04	-5.3625070189e-04
4	2.8889192e-07	2.8889213e-07	-2.8889192834e-04	-2.8889213997e-04
6	-5.8675941e-07	-5.8676048e-07	-3.1677933271e-04	-3.1677940016e-04

IV.A. Adjoint-Based Robust Design Under Aleatory Uncertainty

Design optimization seeks to minimize some quantity (e.g., dBA, PLdB, etc.) written as:

$$\min J(\boldsymbol{D}) \qquad (10)$$

where $\boldsymbol{D}$ is a vector of the design variables. For deterministic design, J is simply the objective of interest. For a stochastic process, the objective is also a function of the uncertain variables. With uncertainty, the formulation of J must be changed to account for variation in the system due to the random variables.

Design under uncertainty is based on performing optimization with an objective composed of mean and standard deviation of the objective. One such approach is known as *robust design*. The objective for robust design is to reduce not only the mean of the design quantity, but also the standard deviation. The robust design objective used in this study (see Eq. (1)) is suitable for systems that possess inherent or aleatory uncertainty due to random variations in the physical system. Adjoint-based design requires calculation of the objective gradients with respect to the design variables, as shown in Eq. (11).

$$\frac{dJ}{d\boldsymbol{D}} = \frac{d\mu}{d\boldsymbol{D}} + \frac{d\sigma}{d\boldsymbol{D}} \qquad (11)$$

One of the significant challenges with design under uncertainty is the computational cost of propagating the uncertainty at each optimization step. Traditional sampling approaches may require a significant number of evaluations of the deterministic model to obtain converged statistics. When the deterministic model is complicated as in the case of CFD-based design, traditional sampling techniques may become impractical. To relax the computational burden, a surrogate modeling approach may be used as a means of efficient uncertainty propagation and quantification.

IV.B. Point-Collocation Non-intrusive Polynomial Chaos

In recent studies,[20,21,22,23,24] the polynomial chaos method has been favored as a means of uncertainty quantification (UQ) over traditional methods such as Monte Carlo, due to its computational efficiency.

American Institute of Aeronautics and Astronautics

Polynomial chaos is a surrogate modeling technique based on a spectral representation of uncertainty. An important aspect of this representation is that a response value or random function Y can be separated into deterministic and stochastic components, as shown in Eq. (12).

$$Y(\boldsymbol{\xi}, \boldsymbol{D}) \approx \sum_{i=0}^{P} \alpha_i(\boldsymbol{D}) \Psi_i(\boldsymbol{\xi}) \tag{12}$$

Here, α_i is the deterministic component and Ψ_i are the random variable basis functions corresponding to the ith mode. The response Y is a function of the independent, random variables $\boldsymbol{\xi}$, and design variables $\boldsymbol{D}$. Note that this series is, by definition, an infinite series. However, in practice it is truncated, and a discrete sum is taken over a number of output modes.[25] To form a complete basis for a total order expansion, N_t terms are required, which can be computed from Eq. (13) for a polynomial chaos expansion (PCE) of order s ($s = 2$ in this study) and a number of random variables, n.

$$N_t = P + 1 = \frac{(n+s)!}{n!s!} \tag{13}$$

Further details on polynomial chaos theory are given by Ghanem[26] and Eldred.[25]

To determine the expansion coefficients α_i, polynomial chaos methods can be implemented by using an intrusive or non-intrusive approach. The intrusive mthod, while appearing straightforward, has been shown to be computationally expensive for complicated problems.[20] As a result, this work applies the non-intrusive approach for which modification of the deterministic model is unnecessary, and that requires only the response values at selected sample points to approximate the stochastic response surface.

IV.B.1. General Approach to Point-Collocation

Several methods have been developed for non-intrusive polynomial chaos (NIPC). Of these, point-collocation NIPC has been used extensively in aerospace simulations and CFD problems.[21, 22, 24, 27] The point-collocation method starts with replacement of a stochastic response with its PCE according to Eq. (12). N_t vectors are then chosen in random space, and the deterministic code is evaluated at these points, which form the left hand side of Eq. (12). Following this, a linear system of N_t equations can be formulated and solved for the spectral modes of the random variables. This system is shown in Eq. (14).

$$\begin{pmatrix} \Psi_0(\boldsymbol{\xi}_0) & \Psi_1(\boldsymbol{\xi}_0) & \cdots & \Psi_P(\boldsymbol{\xi}_0) \\ \Psi_0(\boldsymbol{\xi}_1) & \Psi_1(\boldsymbol{\xi}_1) & \cdots & \Psi_P(\boldsymbol{\xi}_1) \\ \vdots & \vdots & \ddots & \vdots \\ \Psi_0(\boldsymbol{\xi}_P) & \Psi_1(\boldsymbol{\xi}_P) & \cdots & \Psi_P(\boldsymbol{\xi}_P) \end{pmatrix} \begin{pmatrix} \alpha_0 \\ \alpha_1 \\ \vdots \\ \alpha_P \end{pmatrix} = \begin{pmatrix} Y(\boldsymbol{D}, \boldsymbol{\xi}_0) \\ Y(\boldsymbol{D}, \boldsymbol{\xi}_1) \\ \vdots \\ Y(\boldsymbol{D}, \boldsymbol{\xi}_P) \end{pmatrix} \tag{14}$$

Note that for this linear system, N_t is the minimum number of deterministic samples required to obtain an analytical solution (i.e., the coefficient vector). If more samples are available and are linearly independent, the system is overdetermined and can be solved using a least squares approach. The number of samples over the required minimum is represented by the use of an oversampling ratio (OSR), defined as the ratio of the number of actual samples to the minimum number required (N_t). In general, the number of collocation points can be determined by multiplying Eq. (13) by an OSR. Hosder et al.[28] determined an effective OSR of 2.0 for the stochastic model problems studied and showed that the accuracy of the PCE is dependent on the number of collocation points.

IV.B.2. Gradient-Enhanced Point-Collocation

The general point-collocation approach can be extended to include gradients for the calculation of the expansion coefficients.[27, 29, 30] In surrogate modeling, this is commonly referred to as *gradient enhancement*. When using the point-collocation NIPC approach, the gradient formulation can be developed by first differentiating Eq. (12) with respect to the jth standard random variable, as shown in Eq. (15)

$$\frac{\partial Y(\boldsymbol{D}, \boldsymbol{\xi})}{\partial \xi_j} \approx \sum_{i=0}^{P} \alpha_i(\boldsymbol{D}) \frac{\partial \Psi_i(\boldsymbol{\xi})}{\partial \xi_j} \tag{15}$$

American Institute of Aeronautics and Astronautics

Expanding the LHS by noting the standard random variable $\boldsymbol{\xi}$ is a function of the actual random variable $\mathbf{x}$ yields Eq. (16).

$$\frac{\partial Y(\boldsymbol{D}, \boldsymbol{\xi})}{\partial x_j} \frac{\partial x_j}{\partial \xi_j} \approx \sum_{i=0}^{P} \alpha_i(\boldsymbol{D}) \frac{\partial \Psi_i(\boldsymbol{\xi})}{\partial \xi_j} \tag{16}$$

Note that the first term on the LHS is the derivative obtained from a local sensitivity analysis. The next term is based on the known distribution of the uncertain input variable. A normally distributed variable with mean μ and standard deviation σ is shown in Eq. (17).

$$x_i = \sigma \xi_i + \mu \rightarrow \frac{\partial x_i}{\partial \xi_i} = \sigma \tag{17}$$

The differentiated PCE with respect to each uncertain variable at each sample point (Eq. (16)) can be appended to the linear system of Eq. (14). The new system of linear equations is shown in Eq. (18). Note that for N_S sample points, n number of random variables, and N_t terms in the PCE, the dimensions of the coefficient matrix are $N_S(n+1)$ by N_t, the solution vector has dimension $N_S(n+1)$, and the unknown vector has dimension N_t.

$$\begin{pmatrix} \Psi_0(\boldsymbol{\xi}_0) & \Psi_1(\boldsymbol{\xi}_0) & \cdots & \Psi_P(\boldsymbol{\xi}_0) \\ \frac{\partial \Psi_0(\boldsymbol{\xi}_0)}{\partial \xi_1} & \frac{\partial \Psi_1(\boldsymbol{\xi}_0)}{\partial \xi_1} & \cdots & \frac{\partial \Psi_P(\boldsymbol{\xi}_0)}{\partial \xi_1} \\ \vdots & \vdots & \ddots & \vdots \\ \frac{\partial \Psi_0(\boldsymbol{\xi}_0)}{\partial \xi_n} & \frac{\partial \Psi_1(\boldsymbol{\xi}_0)}{\partial \xi_n} & \cdots & \frac{\partial \Psi_P(\boldsymbol{\xi}_0)}{\partial \xi_n} \\ \Psi_0(\boldsymbol{\xi}_1) & \Psi_1(\boldsymbol{\xi}_1) & \cdots & \Psi_P(\boldsymbol{\xi}_1) \\ \frac{\partial \Psi_0(\boldsymbol{\xi}_1)}{\partial \xi_1} & \frac{\partial \Psi_1(\boldsymbol{\xi}_1)}{\partial \xi_1} & \cdots & \frac{\partial \Psi_P(\boldsymbol{\xi}_1)}{\partial \xi_1} \\ \vdots & \vdots & \ddots & \vdots \\ \frac{\partial \Psi_0(\boldsymbol{\xi}_1)}{\partial \xi_n} & \frac{\partial \Psi_1(\boldsymbol{\xi}_1)}{\partial \xi_n} & \cdots & \frac{\partial \Psi_P(\boldsymbol{\xi}_1)}{\partial \xi_n} \\ \vdots & \vdots & \ddots & \vdots \\ \vdots & \vdots & \ddots & \vdots \\ \Psi_0(\boldsymbol{\xi}_{N_s-1}) & \Psi_1(\boldsymbol{\xi}_{N_s-1}) & \cdots & \Psi_P(\boldsymbol{\xi}_{N_s-1}) \\ \frac{\partial \Psi_0(\boldsymbol{\xi}_{N_s-1})}{\partial \xi_1} & \frac{\partial \Psi_1(\boldsymbol{\xi}_{N_s-1})}{\partial \xi_1} & \cdots & \frac{\partial \Psi_P(\boldsymbol{\xi}_{N_s-1})}{\partial \xi_1} \\ \vdots & \vdots & \ddots & \vdots \\ \frac{\partial \Psi_0(\boldsymbol{\xi}_{N_s-1})}{\partial \xi_n} & \frac{\partial \Psi_1(\boldsymbol{\xi}_{N_s-1})}{\partial \xi_n} & \cdots & \frac{\partial \Psi_P(\boldsymbol{\xi}_{N_s-1})}{\partial \xi_n} \end{pmatrix} \begin{pmatrix} \alpha_0 \\ \alpha_1 \\ \alpha_2 \\ \vdots \\ \vdots \\ \vdots \\ \vdots \\ \vdots \\ \vdots \\ \vdots \\ \vdots \\ \vdots \\ \vdots \\ \alpha_P \end{pmatrix} = \begin{pmatrix} Y(\boldsymbol{D}, \boldsymbol{\xi}_0) \\ \frac{\partial Y(\boldsymbol{D}, \boldsymbol{\xi}_0)}{\partial x_1} \frac{\partial x_1}{\partial \xi_1} \\ \vdots \\ \frac{\partial Y(\boldsymbol{D}, \boldsymbol{\xi}_0)}{\partial x_n} \frac{\partial x_N}{\partial \xi_n} \\ \frac{\partial Y(\boldsymbol{D}, \boldsymbol{\xi}_1)}{\partial x_1} \frac{\partial x_1}{\partial \xi_1} \\ \vdots \\ \frac{\partial Y(\boldsymbol{D}, \boldsymbol{\xi}_1)}{\partial x_n} \frac{\partial x_N}{\partial \xi_n} \\ \vdots \\ \vdots \\ Y(\boldsymbol{D}, \boldsymbol{\xi}_{N_s-1}) \\ \frac{\partial Y(\boldsymbol{D}, \boldsymbol{\xi}_{N_s-1})}{\partial x_1} \frac{\partial x_1}{\partial \xi_1} \\ \vdots \\ \frac{\partial Y(\boldsymbol{D}, \boldsymbol{\xi}_{N_s-1})}{\partial x_n} \frac{\partial x_n}{\partial \xi_n} \end{pmatrix} \tag{18}$$

The derivatives of the basis polynomials in the LHS of Eq. (18) can be obtained either analytically or through finite differencing. The solution procedure is no different than that used for the original point-collocation scheme. However, this modified scheme makes use of gradients, which can be obtained through sensitivity analysis. This approach has the advantage of reducing the number of samples needed to construct the surrogate model and promise to reduce the computational cost of computing sensitivities with respect to the uncertain variables.

IV.B.3. *Sparse Approximation*

Polynomial chaos techniques suffer from the curse of dimensionality. That is, the number of deterministic model evaluations required to create an accurate surrogate model grows exponentially with the number of random dimensions. For many large-scale, complicated problems, the minimum required number of deterministic model samples may be impractical or even impossible to obtain. An ideal approach would achieve an accurate surrogate model with as few deterministic samples as possible, even if the minimum number of samples required for a total order expansion (Eq. (13)) is not achievable. The next subsection describes an underdetermined solution approach that will achieve accuracy in the surrogate model while reducing the cost of deterministic evaluations.

American Institute of Aeronautics and Astronautics

In general, a system of linear equations that has fewer linearly independent equations than unknowns possesses an infinite number of solutions. In many PCEs, only a small fraction of the coefficients may carry significant weight in the surrogate model. This allows for an assumption that many of the expansion coefficients are zero, making the vector of expansion coefficients sparse. Under this assumption, the linear system can be regularized, which allows for a well-posed problem. The objective is to seek a solution to the linear system with the fewest number of non-zero coefficients. By using convex relaxation, a solution can be obtained from the L_1-minimization problem shown in Eq. (19).

$$\min \left\| \alpha \right\|_1 \text{ subject to } \left\| \Psi\alpha - Y \right\|_2 \leq \delta \tag{19}$$

Here, δ is the truncation error associated with the truncation of the series in Eq. (12). For problems in this study, δ is assumed to be near zero, as it can be shown that the solution to Eq. (19) is unique in this instance. In the above formulation, the dimensions of Ψ are N_s by N_t and the vector α^* is of length N_s, with $N_s < N_t$ for the underdetermined problem. The vector α is of length N_t. Doostan and Owhadi[31] discuss, in great detail, the theory and formulation of the above method, as well as its stability.

The optimization problem in Eq. (19) is commonly referred to as Basis Pursuit Denoising (BPDN),[31,32,33] and can be solved using methods from quadratic programming.[32,33] In the current study, the least absolute shrinkage and selection operator (LASSO) homotopy optimization routine[33] was selected to find the optimal solution of Eq. (19). While many methods exist for solving the above minimization problem, the homotopy method was selected for efficiency, as this method is not significantly affected by the dimensionality of the problem.[32]

IV.C. Moments and Design Variable Sensitivities

Adjoint-based design under uncertainty requires that statistical moments and gradient information with respect to the design variables be determined. Eldred[25] shows that with polynomial chaos, moments can be determined analytically, as shown in Eqs. (20) and (21) for the mean and variance of the stochastic expansion.

$$\mu_Y = \langle Y \rangle \approx \sum_{i=0}^{P} \alpha_i(\boldsymbol{D}) \langle \Psi_i(\boldsymbol{\xi}) \rangle = \alpha_0 \tag{20}$$

$$\sigma_Y^2 = \langle (Y - \mu_Y)^2 \rangle \approx \langle (\sum_{i=0}^{P} \alpha_i(\boldsymbol{D}) \Psi_i(\boldsymbol{\xi}))^2 \rangle = \sum_{i=1}^{P} \alpha_i^2(\boldsymbol{D}) \langle \Psi_i^2(\boldsymbol{\xi}) \rangle \tag{21}$$

The robust design objective in Eq. (1) can be calculated with these two moments. In this study, because discrete-adjoint gradients are available, the gradient-enhanced point-collation approach is used for computation of the robust objective.

To satisfy the adjoint-based design objective in Eq. (11), moment sensitivities must be obtained. The sensitivity of the mean with respect to the design variables is obtained by differentiating Eq. (20), which is shown in Eq. (22).

$$\frac{d\mu_Y}{d\boldsymbol{D}} = \frac{d}{d\boldsymbol{D}} \langle Y \rangle = \langle \frac{dY}{d\boldsymbol{D}} \rangle \tag{22}$$

This calculation is trivial when the sensitivities of each response with respect to each design variable are known, as it is simply the average of the sensitivities for each design variable. The sensitivity of the variance is shown in Eq. (23), which is obtained by differentiating Eq. (21).

$$\frac{d\sigma_Y^2}{d\boldsymbol{D}} = \sum_{i=1}^{P} \langle \Psi_i^2(\boldsymbol{\xi}) \rangle \frac{d\alpha_j^2}{d\boldsymbol{D}} = 2 \sum_{i=1}^{P} \alpha_j \langle \Psi_i^2(\boldsymbol{\xi}) \rangle \frac{d\alpha_j}{d\boldsymbol{D}} \tag{23}$$

Obtaining the sensitivities in Eq. (23) requires that the sensitivities of the expansion coefficients be determined. A second polynomial chaos expansion can be constructed by differentiating Eq. (12) with respect to the jth design variable, as shown in Eq. (24).

$$\frac{\partial Y(\boldsymbol{D}, \boldsymbol{\xi})}{\partial D_j} \approx \sum_{i=0}^{P} \frac{d\alpha_i(\boldsymbol{D})}{dD_j} \Psi_i(\boldsymbol{\xi}) \tag{24}$$

Solving this equation for sensitivities of the expansion coefficients must be done for each of the design variables and can be accomplished with general point-collocation or the L_1-minimization approach, if the system is underdetermined. The sensitivity-based approach can also be used, but has an added cost of obtaining mixed derivative $\frac{\partial}{\partial \boldsymbol{\xi}}\left(\frac{\partial Y}{\partial \boldsymbol{D}}\right)$.

V. CFD Integration

The boom-adjoint formulation developed here is coupled with the NASA Langley FUN3D[34] unstructured CFD solver. FUN3D solves the steady and unsteady Euler and Reynolds-averaged Navier-Stokes equations on general static and dynamic mixed-element grid discretizations. It has been used for a broad class of aerodynamic analysis and design simulations across the speed range. FUN3D also offers a discretely-consistent adjoint implementation that has been used to perform mathematically-rigorous design optimization,[35,36,37] error estimation, and formal mesh adaptation[38,39] for complex geometries and flow-fields in massively parallel computing environments. In addition, FUN3D offers a discretely-consistent forward mode of differentiation. A scripting procedure[40] can be used to automatically convert the baseline source code to a complex-variable formulation.

FUN3D coupling essentially follows the description from earlier work[8] except in the non-deterministic case, where the sensitivities are separated into two components: those with respect to the deterministic shape variables (D) and those with respect to uncertain atmospheric parameters ($\boldsymbol{\xi}$). The flowchart of the CFD integration used in this study is depicted in Fig. 5, where it is assumed that the number of sBOOM propagation runs needed to quantify the uncertainty is less than the computational nodes used for the simulation; this need not be the case in general. To start the process, the underlying concept is gridded and parameterized. Employing efficient decomposition algorithms, the grid is spread across a computational cluster consisting of E nodes and the flow or adjoint solver is run. Inter-nodal communication is used to maintain the integrity of the complete domain solution. Probability distributions are placed on the uncertain variables and latin hypercube sampling is used to generate $F = 2(nt + nh + nwx + nwy) + 1$ atmospheric profiles, each of which is propagated to the ground in an "embarrassingly parallel" fashion by using a subset/superset of the computational nodes allocated to run the flow/adjoint solvers. After successful completion of sBOOM runs, the objectives and sensitivities, both with respect to deterministic and non-deterministic variables, are passed to the uncertainty quantification algorithm, which then computes the non-deterministic objective values along with their corresponding sensitivities. This information is gathered by the optimizer and used to update the shape parameters for the next iteration of gradient optimization.
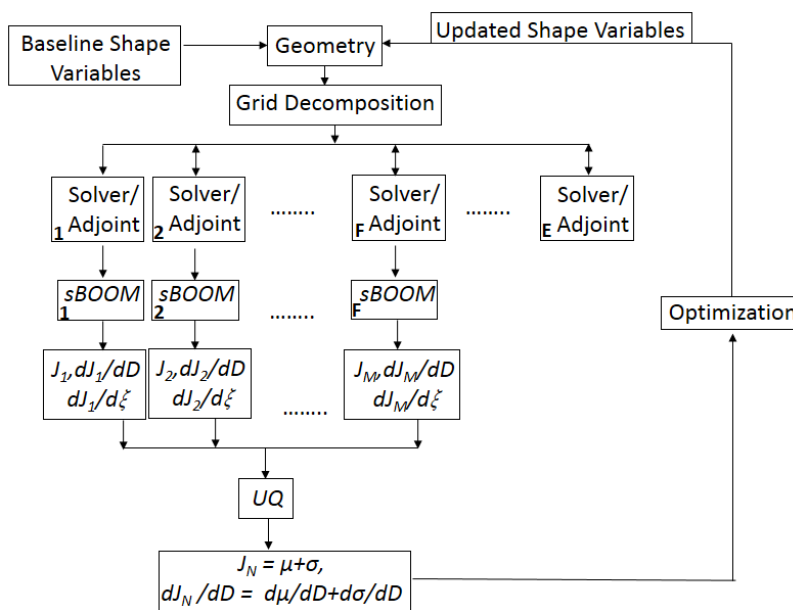

Figure 5. Flowchart of FUN3D-sBOOM-UQ integration.

American Institute of Aeronautics and Astronautics

VI.   Optimization Problem and Setup

The adjoint formulation described in this study is applied to an axisymmetric body of revolution in supersonic flow with free-stream Mach number of 1.6, and angle of attack of 0.6 deg. The initial mesh for this body is generated using VGRID[41] and SSGRID.[42] The grid generation approach employs a heuristic technique to align the mesh topology *a priori* with the expected primary off-body shock structures. A more rigorous adjoint-based approach to mesh adaptation for such problems is described in literature[43] . The near-field is extracted at an off-body distance of 450 ft below the aircraft, which translates to 3 body-lengths. The objective is to reduce the A-weighted loudness of the sonic boom signatures at the ground level with and without consideration of uncertain atmospheric effects. An Euler solver is used in this study as viscous effects are likely to be small for boom minimization purposes.

The surface mesh for the axisymmetric body is parameterized by using the BANDAIDS[44] free-form shape deformation tool. BANDAIDS provides a compact set of design variables for modifying a discrete surface mesh in the normal direction, along with analytic sensitivities required by the discrete adjoint formulation of the near-field CFD problem. The parameters for shape modification are NURBS control points. However, to make smooth changes to the underlying mesh and reduce the number of variables, all control points at constant-x are grouped to allow radial expansion or contraction of that station by a single variable. After grouping, there are a total of 25 design variables for modifying the concept, with only 21 allowed to very during optimization. Because of compact support of NURBS basis functions, deformations at any section smoothly deforms the underlying mesh up to two adjacent stations on either side of the location being deformed. The primary criteria in the choice of parameterization was to balance the number of design variables with deformation smoothness. The SNOPT optimization package[45] was used to perform shape optimization.

VII.   Results and Discussion

This section presents the shape optimization results of both the deterministic and robust optimization approaches, and results from each are discussed.

VII.A.   Deterministic Optimization

A deterministic unconstrained optimization is initially run to minimize the A-weighted loudness obtained using standard atmospheric profiles. Figure 6(a) shows the changes to the geometry after optimization compared to the baseline while Fig. 6(b) depicts cross-sectional comparison along a few non-dimensional longitudinal locations represented by η. The solid (red) lines represent the baseline and the dash-dotted (blue) lines represent the optimum configuration. The optimizer shrinks the radius at the front and aft sections while enlarging the middle portion. Figures 7(a) and 7(b) compare the near-field and ground signatures, respectively. In the near-field, the initial shock strength is significantly reduced, followed by a gradual pressure increase to the maximum. Shaping eliminates the middle shock, both in the near-field and the ground signature. The ground signature changes from a three-strong-shock solution to an essentially sinusoidal shape, with a reduction from 82.8 to 66.1 on the perceived level scale[46] or from 68.6 to 53.5 on the A-weighted loudness scale.

VII.B.   Robust Design Optimization

To simplify the problem and reduce the dimensionality during robust optimization, fewer points in the lateral wind and relative humidity profiles are used as shown in Tables 10 and 11, respectively. This reduces the number of uncertain variables to 30. Normal distributions are placed on these variables with means and standard deviations listed in Table 12.

Robust optimization starts from the same baseline geometry used to start the deterministic optimization. The optimization reaches a mean and standard deviation of 53.28 and 1.07, respectively. The iteration histories of both optimization runs are compared in Fig. 8, where the need to evaluate the robustness measures of the objective has increased the number of function evaluations by more than a factor of two.

Figure 9 compares the cross-section shapes after robust optimization with those resulting from the deterministic optimization at the quoted η locations. Side-views of the two optimized geometries are also shown in the figure, where an axis ratio of $Y/X = 50$ is chosen to emphasize cross-sectional differences. The
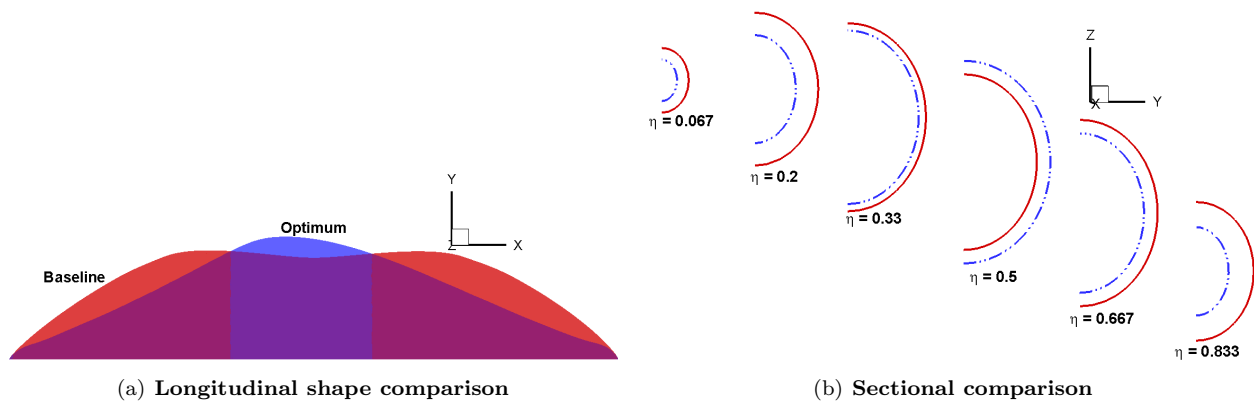
American Institute of Aeronautics and Astronautics

(a) **Longitudinal shape comparison**

(b) **Sectional comparison**

Figure 6. Shape changes after deterministic optimization

(a) **Comparison of $\Delta p/P$ at $h/L = 3$**
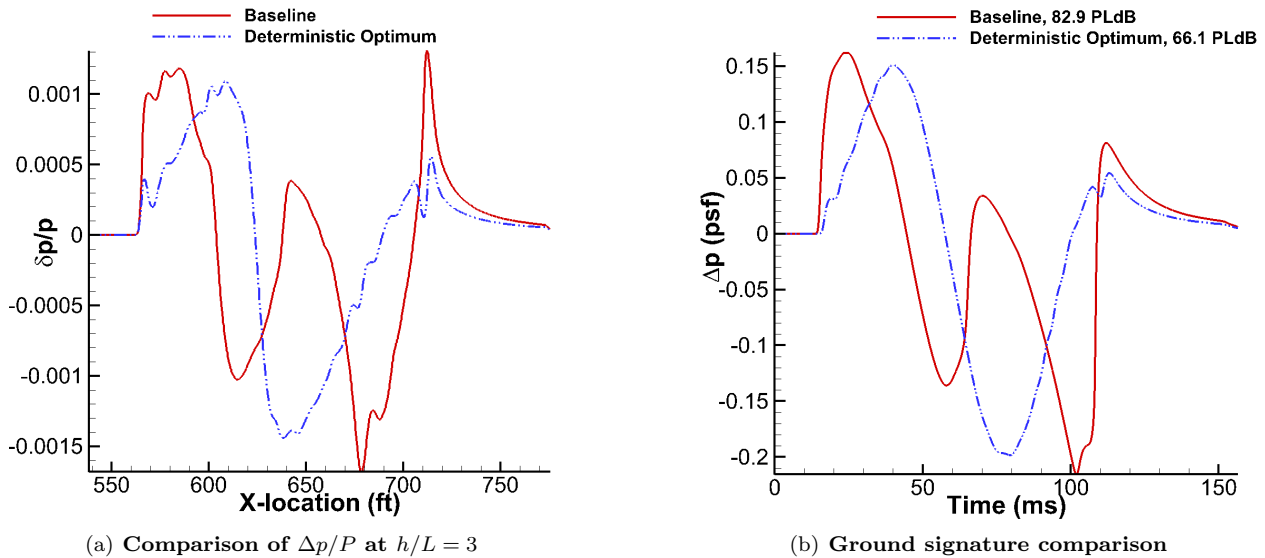
(b) **Ground signature comparison**

Figure 7. Near-field and ground signature comparison after deterministic optimization

Table 10. Atmospheric Y-wind table.

i	Altitude (m)	Y-Wind (m/s)
1	0.0	0.0
2	5000.0	10.0
3	20000.0	20.0

Table 11. Atmospheric Relative Humidity table.

i	Altitude (m)	RH $(\%)$
1	0.0	59.62
2	1520.0	67.06
3	6400.0	77.66
4	7620.0	66.96
5	10060.0	24.38
6	13720.0	8.49

cross-sections differ even for this simple axisymmetric body of revolution, where the near-field consists of a single expansion sandwiched between two compression systems.

Figures 10(a) and 10(b) show the near-field and ground signature comparisons after robust design optimization, obtained using a standard atmosphere. The near-field changes visibly, and this results in ground signatures that are slightly different as well. Even though the optimization is run with multiple atmospheric profiles, the ground signature shown here is computed using a standard atmosphere. The mean A-weighted loudness is slightly lower, at 53.28 than the deterministic optimum of 53.52, even though the

American Institute of Aeronautics and Astronautics

Table 12. Atmospheric profile distribution means and standard deviations

Variable	μ	σ	Variable	μ	σ	Variable	μ	σ
H_1	0.0	1.0	ZH_5	10060.0	1000.0	WXH_3	20000.0	1000.0
H_2	11000.0	1000.0	ZH_6	13720.0	1000.0	WX_1	0.0	1.0
H_3	20000.0	1000.0	RH_1	59.62 %	15.0	WX_2	20.0	5.0
T_1	59.0 ^oF	5.0	RH_2	67.06 %	15.0	WX_3	30.0	10.0
T_2	-69.7 ^oF	5.0	RH_3	77.66 %	15.0	WYH_1	0.0	1.0
T_3	-69.7 ^oF	5.0	RH_4	66.96 %	15.0	WYH_2	5000.0	1000.0
ZH_1	0.0	1.0	RH_5	24.38 %	10.0	WYH_3	20000.0	1000.0
ZH_2	1520.0	500.0	RH_6	8.49 %	5.0	WY_1	0.0	1.0
ZH_3	6400.0	1000.0	WXH_1	0.0	1.0	WY_2	10.0	5.0
ZH_4	7620.0	1000.0	WXH_2	5000.0	1000.0	WY_3	20.0	10.0
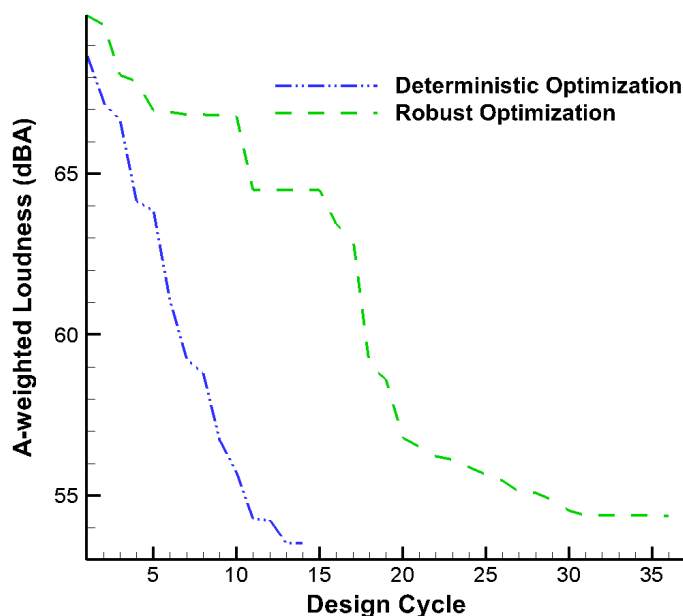
Figure 8. Comparison of iteration histories of deterministic and robust optimizations

loudness calculated using the standard atmospheric profile at the robust optimum point is slightly higher at 53.62. The perceived level follows the same trend as the A-weighted loudness owing to the correlation between the two metrics.[47] The peak overpressure of the robust signature is reduced compared to the deterministic case; however owing to the smaller rise-time to peak over-pressure of the initial shock, the loudness is slightly higher. Nevertheless, signature variability due to different atmospheres is taken into account during optimization, yielding a design robust to atmospheric changes.

The probability distributions of the A-weighted loudness level on the ground before and after robust design optimization are plotted in Fig. 11. As expected, the current formulation simultaneously reduces the mean by shifting the curve to the left, as well as the standard deviation by making the distribution sharper.

VIII.   Summary

A methodology to tackle propagation uncertainty during sonic boom minimization has been developed by using a discrete adjoint approach. The formal coupling between the boom adjoint method and CFD has been enhanced for robust shape optimization of low-boom supersonic aircraft concepts by using a non-intrusive polynomial chaos formulation. This approach complements other advanced conceptual design methods for boom mitigation by providing uncertainty bounds on optimized designs. The methodology has been applied
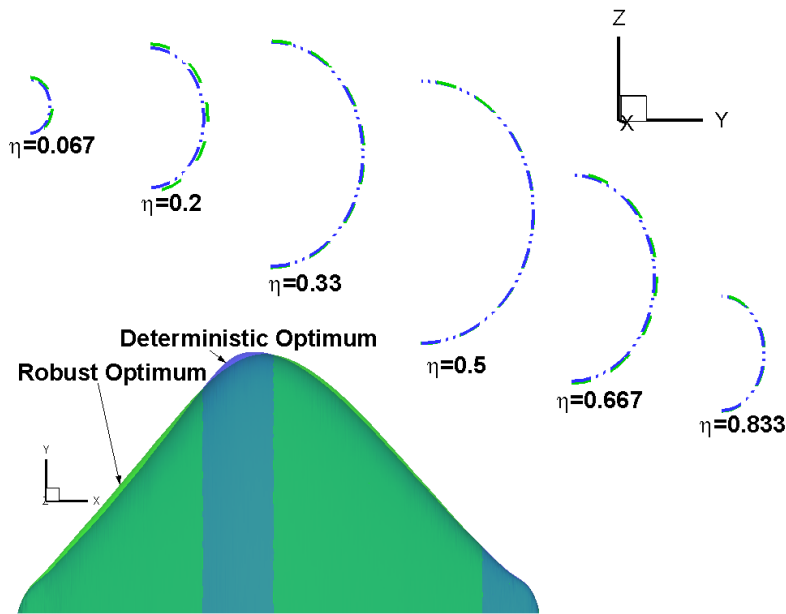
American Institute of Aeronautics and Astronautics

Figure 9. Sectional changes after robust optimization compared to deterministic optimum

(a) **Comparison of $\Delta p/P$ at $h/L = 3$**
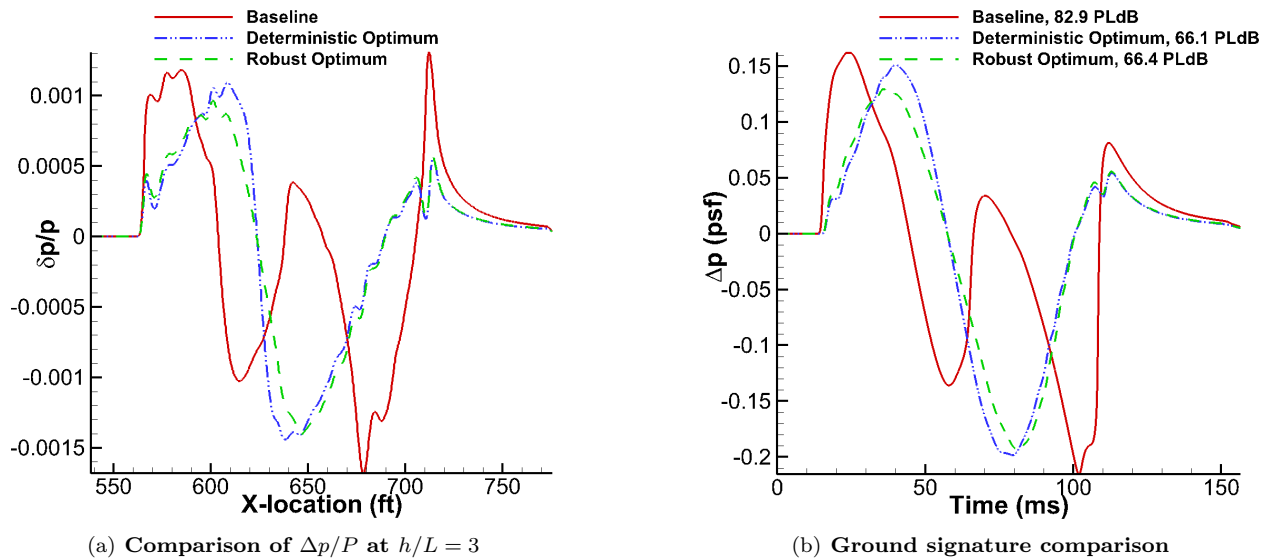
(b) **Ground signature comparison**

Figure 10. Near-field and ground signature comparison after robust optimization

to an axisymmetric body to perform both deterministic and robust optimization. The results showed that robust optimization produced a different optimum, with a shape that accounted for atmospheric variability. Two major benefits are achieved by using the approach described in this paper. The first benefit is the simultaneous minimization of the mean and standard deviation, which will become more important as more uncertain atmospheric parameters are included. The second benefit is that the approach is computationally efficient through the use of a non-intrusive polynomial chaos formulation that samples a surrogate instead of the actual analysis and provides analytical sensitivities of the underlying surrogate for use in gradient-based optimization. In addition, using the boom loudness on the ground as the objective in shape optimization has the advantage of removing the need for near-field or equivalent area targets, which are required for other shape optimization approaches to mitigate sonic boom. Future work will apply this methodology to a complex aircraft concept.

American Institute of Aeronautics and Astronautics
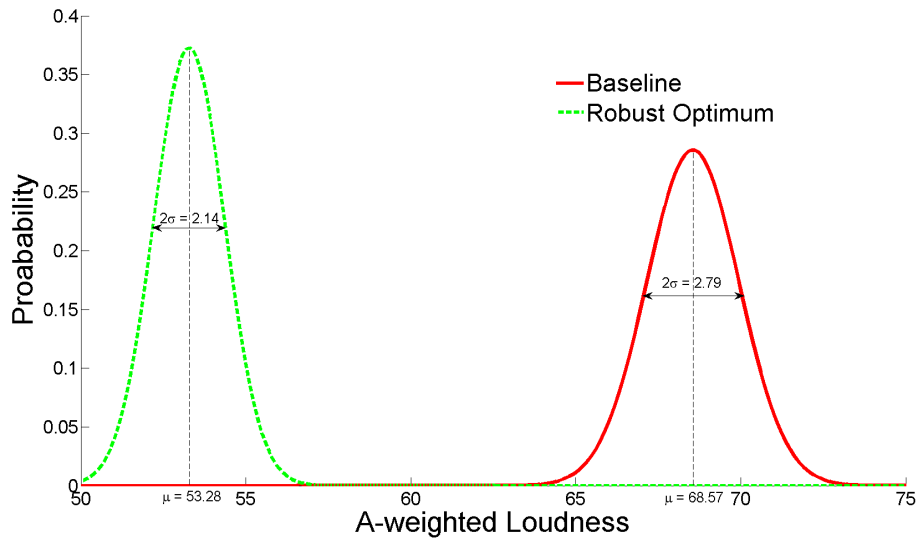
Figure 11. Probability distributions before and after robust optimization.

Acknowledgments

Appendix

The tridiagonal matrices for the relaxation processes are:

$$A^n, A_2^n = \begin{pmatrix} 1 & 0 & \cdots & & & \\ 0 & 1 & 0 & \cdots & & \\ 0 & -\alpha\kappa_1 - \kappa_2 & (1+2\alpha\kappa_1) & \kappa_2 - \alpha\kappa_1 & \cdots & \\ & \ddots & & \ddots & & \ddots \\ & & \cdots & & 0 & 1 & 0 \\ & & \cdots & & & 0 & 1 \end{pmatrix}$$

$$B^n, B_2^n = \begin{pmatrix} 1 & 0 & \cdots & & & \\ 0 & 1 & 0 & \cdots & & \\ 0 & \alpha'\kappa_1 - \kappa_2 & (1-2\alpha'\kappa_1) & \kappa_2 + \alpha'\kappa_1 & \cdots & \\ & \ddots & & \ddots & & \ddots \\ & & \cdots & & 0 & 1 & 0 \\ & & \cdots & & & 0 & 1 \end{pmatrix}$$

In the above matrices, $\kappa_1 = \frac{C_\nu \Delta\chi_n}{\Delta\tau^2}$, $\kappa_2 = \frac{\theta_\nu}{2\Delta\tau}$, and $\alpha' = 1 - \alpha$. If using the Crank-Nicholson scheme, $\alpha = 0.5$. For thermo-viscous absorption, the matrices are given below with $\lambda = \frac{\Delta\chi_n}{2\Gamma(\Delta\tau)^2}$

$$A_3^n = \begin{pmatrix} 1 & 0 & \cdots & \\ -\lambda & (1+2\lambda) & -\lambda & \cdots \\ & \ddots & \ddots & \ddots \\ & & \cdots & 0 & 1 \end{pmatrix}$$

American Institute of Aeronautics and Astronautics

$$B_3^n = \begin{pmatrix} 1 & 0 & \cdots & & \\ \lambda & (1-2\lambda) & \lambda & \cdots & \\ & \ddots & & \ddots & \ddots \\ & & & \cdots & 0 & 1 \end{pmatrix}$$

References

[1] Pawlowski, J. W., Graham, D. H., et al., "Origins and Overview of the Shaped Sonic Boom Demonstration Program," AIAA Paper 2005-5, Jan. 2005.

[2] Aftosmis, M., Nemec, M., and Cliff, S., "Adjoint-based Low-Boom Design with Cart3D (Invited)," AIAA Paper 2011-3500, June 2011.

[3] Howe, D., Simmons, F., and Freund, D., "Development of the Gulfstream Quiet Spike ^{TM} for Sonic Boom Minimization," AIAA Paper 2008-0124, Jan. 2008.

[4] Morgenstern, J., Norstrud, N., Stelmack, M., and Skoch, C., "Final Report for the Advanced Concept Studies for Supersonic Commercial Transports Entering Service in the 2030 to 2035 Period, N+3 Supersonic Program,," Tech. Rep. CR-2010-216796, PMF-01623, E-17427,Document ID 20100036507, National Aeronautics and Space Administration, Langley, Virginia, Oct. 2010.

[5] Palacios, F., Alonso, J. J., Colonno, M., Hicken, J., and Lukaczyk, T., "Adjoint-Based method for supersonic aircraft design using equivalent area distribution," AIAA Paper 2012-0269, Jan. 2012.

[6] Magee, T. E., Shaw, S. G., and Fugal, S. R., "Experimental Validations of a Low-Boom Aircraft Design," AIAA Paper 2013-0646, Jan. 2013.

[7] Morgenstern, J. M., "Tail-braced wing aircraft and configurations for achieving long supersonic range and low sonic boom," US Patent No. 6729577, Lockheed Martin Corporation, May 2004.

[8] Rallabhandi, S. K., Nielsen, E. J., and Diskin, B., "Sonic-Boom Mitigation Through Aircraft Design and Adjoint Methodology," *Journal of Aircraft*, Vol. 51, No. 2, 2014, pp. 502–510.

[9] Rallabhandi, S. K., "Application of Adjoint Methodology to Supersonic Aircraft Design Using Reversed Equivalent Areas," *Journal of Aircraft*, Vol. 51, No. 6, 2014, pp. 1873–1882.

[10] Nadarajah, S., Jameson, A., and Alonso, J., "Sonic Boom Reduction using an Adjoint Method for Wing-Body Configurations in Supersonic Flow," AIAA Paper 2002-5547, Sept. 2002.

[11] Wintzer, M. and Kroo, I., "Optimization and Adjoint-Based CFD for the Conceptual Design of Low Sonic Boom Aircraft," AIAA Paper 2012-0963, Jan. 2012.

[12] "U.S. Standard Atmosphere," *U.S. Government Printing Office, Washington, D.C.*, 1976.

[13] Rallabhandi, S. K., "Advanced Sonic Boom Prediction Using Augmented Burger's Equation," *Journal of Aircraft*, Vol. 48, No. 4, 2011, pp. 1245–1253.

[14] West, T., Reuter, B., Walker, E., Kleb, W. L., and Park, M. A., "Uncertainty Quantification and Certification Prediction of Low-Boom Supersonic Aircraft Configurations," AIAA Paper 2014-2139, June 2014.

[15] Plotkin, K. J., "State of the Art of Sonic Boom Modeling," *Journal of Acoustical Society of America*, Vol. 111, No. 1, Jan. 2002, pp. 530–535.

[16] Onyeonwu, R. O., "The Effects of Wind and Temperature Gradients on Sonic Boom Corridors," *UTIAS Technical Note 168*, October, 1971.

[17] Committee S1, Acoustics, "Method for Calculation of the Absorption of Sound by the Atmosphere, Annex C," ANSI Standard S1.26-1995, American National Standards Institute, New York, NY, September 1995.

[18] Lyness, J. N., "Numerical Algorithms Based on the Theory of Complex Variables," *Proceedings of the ACM 22nd National Conference*, 1967, pp. 124–134.

[19] Lyness, J. N. and Moler, C. B., "Numerical Differentiation of Analytic Functions," *SIAM Journal on Numerical Analysis*, Vol. 4, 1967, pp. 202–210.

[20] Hosder, S. and Bettis, B., "Uncertainty and Sensitivity Analysis for Reentry Flows with Inherent and Model-Form Uncertainties," *Journal of Spacecraft and Rockets*, Vol. 49, No. 2, 2012, pp. 193–206.

[21] Bettis, B., Hosder, S., and Winter, T., "Efficient Uncertainty Quantification in Multidisciplinary Analysis of a Reusable Launch Vehicle," AIAA 2011-2393, April 2011.

[22] Hosder, S., Walters, R. W., and Balch, M., "Point-Collocation Nonintrusive Polynomial Chaos Method for Stochastic Computational Fluid Dynamics," *AIAA Journal*, Vol. 48, No. 12, 2010, pp. 2721–2730.

[23] Witteveen, J. A. S. and Bijl, H., "Efficient Quantification of the Effect of Uncertainties in Advection-Diffusion Problems Using Polynomial Chaos," *Numerical Heat Transfer*, Vol. 53, No. 5, 2008, pp. 437–465.

[24] Han, D. and Hosder, S., "Inherent and Model-Form Uncertainty Analysis for CFD Simulation of Synthetic Jet Actuators," AIAA 2012-0082, Jan. 2012.

[25] Eldred, M. S., "Recent Advances in Non-Intrusive Polynomial Chaos and Stochastic Collocation Methods for Uncertainty Analysis and Design," AIAA 2009-2274, May 2009.

[26] Ghanem, R. G. and Spanos, P. D., *Stochastic Finite Elements: A Spectral Approach*, Springer-Verlag, New York, 1991.

[27] West IV, T. K., Hosder, S., and Johnston, C. O., "Multi-Step Uncertainty Quantification Approach Applied to Hypersonic Reentry Flows," *Journal of Spacecraft and Rockets*, Vol. 51, No. 1, 2014, pp. 296–310.

[28] Hosder, S., Walters, R. W., and Balch, M., "Efficient Sampling for Non-Intrusive Polynomial Chaos Applications with Multiple Uncertain Input Variables," AIAA 2007-1939, April 2007.

American Institute of Aeronautics and Astronautics

[29]Lockwood, B. and Mavriplis, D., "Gradient-Based Methods for Uncertainty Quantification in Hypersonic Flows," *Computers and Fluids*, Vol. 85, No. 1, Oct. 2013, pp. 27–38.

[30]Roderick, O., Anitescu, M., and Fischer, P., "Polynomial Regression Approaches Using Derivative Information for Uncertainty Quantification," *Nuclear Science and Engineering*, Vol. 164, No. 2, 2010, pp. 122–139.

[31]Doostan, A. and Owhadi, H., "A non-adapted sparse approximation of PDEs with stochastic inputs," *Journal of Computational Physics*, Vol. 230, No. 8, 2011, pp. 3015–3034.

[32]Yang, A., Ganesh, A., Sastry, S., and Ma, Y., "Fast L1-Minimization Algorithms and An Application in Robust Face Recognition: A Review," Tech. Rep. UCB/EECS-2010-13, EECS Department, University of California, Berkeley, Feb 2010.

[33]Asif, M. S. and Romberg, J., "Fast and Accurate Algorithms for Re-Weighted l_1-Norm Minimization," *IEEE Transactions on Signal Processing*, Vol. 61, No. 23, 2013, pp. 5905–4916.

[34]Nielsen, E. J. et al., "FUN3D: Fully Unstructured Navier-Stokes," http://fun3d.larc.nasa.gov/, accessed April 2015.

[35]Nielsen, E. J., Diskin, B., and Yamaleev, N. K., "Discrete Adjoint-Based Design Optimization of Unsteady Turbulent Flows on Dynamic Unstructured Grids," *AIAA Journal*, Vol. 48, No. 6, 2010, pp. 1195–1206.

[36]Nielsen, E. and Diskin, B., "Discrete Adjoint-Based Design for Unsteady Turbulent Flows on Dynamic Overset Unstructured Grids," *AIAA Journal*, Vol. 51, No. 6, June 2013, pp. 1355–1373.

[37]Nielsen, E. J. and Jones, W. T., "Integrated Design of an Active Flow Control System Using a Time-Dependent Adjoint Method," *Mathematical Modeling of Natural Phenomena*, Vol. 6, No. 3, 2011, pp. 141–165.

[38]Jones, W. T., Nielsen, E. J., and Park, M. A., "Validation of 3D Adjoint Based Error Estimation and Mesh Adaptation for Sonic Boom Prediction," AIAA Paper 2006-1150, Jan. 2006.

[39]Park, M. A., Lee-Rausch, E. M., and Rumsey, C. L., "FUN3D and CFL3D Computations for the First High Lift Prediction Workshop," AIAA Paper 2011-936, Jan. 2011.

[40]Kleb, W. L., Nielsen, E. J., Gnoffo, P. A., Park, M. A., and Wood, W. A., "Collaborative Software Development in Support of Fast Adaptive Aerospace Tools (FAAST)," AIAA Paper 2003-3978, June 2003.

[41]Pirzadeh, S., "Three-Dimensional Unstructured Viscous Grids by the Advancing-Layers Method," *AIAA Journal*, Vol. 34, No. 1, 1996, pp. 43–49.

[42]Campbell, R. L., Carter, M. B., Deere, K. A., and Waithe, K. A., "Efficient Unstructured Grid Adaptation Methods for Sonic Boom Prediction," AIAA Paper 2008-7327, Aug. 2008.

[43]Park, M. A., "Low Boom Configuration Analysis with FUN3D Adjoint Simulation Framework," AIAA 2011-3337, June 2011.

[44]Samareh, J. A., "Aerodynamic Shape Optimization based on free-form deformation," AIAA Paper 2004-4630, Sept. 2004.

[45]Gill, P. E., Murray, W., and Saunders, M., "SNOPT: Software for Large-Scale Nonlinear Programming," http://www.sbsi-sol-optimize.com/manuals/SNOPTManual.pdf, accessed June 2013.

[46]Stevens, S., "Perceived level of noise by Mark VII and decibels(E)," *Journal of the acoustical society of America*, Vol. 51, No. 2, 1972, pp. 575–601.

[47]Sullivan, B. M., Klos, J., Buehrle, R. D., McCurdy, D. A., and Edward A. Haering, J., "Human Response to Low-Intensity Sonic Booms Heard Indoors and Outdoors," NASA TM 2010-216685, 2010.